Journal of Oceanography, Vol. 64, pp. 691 to 703, 2008

Optical Moorings-of-Opportunity for Validation of Ocean Color Satellites

VICTOR S. KUWAHARA[1]*, GRACE CHANG[2], XIAOBING ZHENG[3], TOMMY D. DICKEY[2] and SONGNIAN JIANG[2]

[1]*Faculty of Education, Soka University, Tokyo 192-8577, Japan*
[2]*Ocean Physics Laboratory, University of California Santa Barbara, 6487 Calle Real Suite A, Goleta, CA 93117, U.S.A.*
[3]*Remote Sensing Department, Anhui Institute of Optics and Fine Mechanics, Hefei, China*

(Received 24 September 2007; in revised form 3 April 2008; accepted 3 April 2008)

Buoy-mooring platforms are advantageous for time-series validation and vicarious calibration of ocean color satellites because of their high temporal resolution and ability to perform under adverse weather conditions. Bio-optical data collected on the Bermuda Testbed Mooring (BTM) were used for comparison with satellite ocean color data in an effort to further standardize sampling and data processing methods for high quality satellite-mooring comparisons. Average percentage differences between satellite-measured and mooring-derived water leaving radiances were about 20% at the blue wavelengths, decreasing to as low as 11% in the blue-green to green wavebands. Based on a series of data processing methods and analyses, recommendations concerning rigor of quality control for collected data, optimal averaging of high-frequency data, sensor self-shading wind corrections, and instrumentation placement requirements are given for the design and application of optical moorings for ocean color satellite validation. Although buoy-mooring platforms are considered to be among the very best methods to validate ocean color satellite measurements, match-up discrepancies due to water column variability and atmospheric corrections remain important issues.

Keywords:
· Optics,
· moorings,
· validation.

1. Introduction

No other type of observational platform has had a greater impact on large-scale, synoptic measurements of the marine biological environment than ocean color satellites. Results obtained from ocean color imaging satellites such as the Nimbus-7 Coastal Zone Color Scanner (CZCS), the Sea-viewing Wide Field-of-view Sensor (SeaWiFS), and the Moderate-Resolution Imaging Spectroradiometer (MODIS) have greatly expanded our knowledge of global distributions of phytoplankton, ocean primary productivity, and biogeochemical fluxes (e.g., Aiken *et al*., 1992; Hooker *et al*., 1992; Behrenfeld and Falkowski, 1997; Campbell *et al*., 2002; Behrenfeld *et al*., 2005). However, determinations of water column properties from satellite platforms are complicated and major improvements and increased information content are still needed for many operational and application purposes. The optimal utilization of ocean color imagers mounted on satellite platforms is constrained by several factors, including the quality and interpretation of the radiometric data sets. Of utmost importance to data quality are the accuracy of the corrections (including quantification of the degradation of optical detectors and atmospheric effects) and the efficacy of ocean color algorithms that are required to relate satellite ocean color measurements to in-water quantities (O'Reilly *et al*., 1998; Fargion and Mueller, 2000; Hooker and McClain, 2000; Pinkerton *et al*., 2003; IOCCG, 2006). Thus, it is critical that remote sensing platforms be complemented with continuous *in situ* measurements to generate and refine the necessary algorithm input parameters for bio-optical products (i.e. Dickey *et al*., 2006).

One of the most successful approaches to validating and vicariously calibrating remotely sensed ocean color data has been the use of *in situ* optical measurements, i.e. ship-based, moored buoys, drifters and profiling floats (Chavez *et al*., 1997; Fargion and Mueller, 2000; Hooker

* Corresponding author. E-mail: victor@soka.ac.jp

Report Documentation Page

Form Approved
OMB No. 0704-0188

1. REPORT DATE	2. REPORT TYPE	3. DATES COVERED
03 APR 2008		**00-00-2008 to 00-00-2008**

4. TITLE AND SUBTITLE	5a. CONTRACT NUMBER
Optical Moorings-of-Opportunity for Validation of Ocean Color Satellites	5b. GRANT NUMBER
	5c. PROGRAM ELEMENT NUMBER
6. AUTHOR(S)	5d. PROJECT NUMBER
	5e. TASK NUMBER
	5f. WORK UNIT NUMBER
7. PERFORMING ORGANIZATION NAME(S) AND ADDRESS(ES) **University of California Santa Barbara,Ocean Physics Laboratory,6487 Calle Real Suite A,Goleta,CA,93117**	8. PERFORMING ORGANIZATION REPORT NUMBER
9. SPONSORING/MONITORING AGENCY NAME(S) AND ADDRESS(ES)	10. SPONSOR/MONITOR'S ACRONYM(S)
	11. SPONSOR/MONITOR'S REPORT NUMBER(S)

12. DISTRIBUTION/AVAILABILITY STATEMENT
Approved for public release; distribution unlimited

13. SUPPLEMENTARY NOTES

14. ABSTRACT

15. SUBJECT TERMS

16. SECURITY CLASSIFICATION OF:			17. LIMITATION OF ABSTRACT	18. NUMBER OF PAGES	19a. NAME OF RESPONSIBLE PERSON
a. REPORT **unclassified**	b. ABSTRACT **unclassified**	c. THIS PAGE **unclassified**	**Same as Report (SAR)**	**13**	

and McClain, 2000; Dickey *et al*., 2001, 2006; Strutton *et al*., 2001; Clark *et al*., 2003; Dickey, 2003; Kuwahara *et al*., 2003; Pinkerton *et al*., 2003). In particular, the Eulerian buoy-mooring observational platform has proven to be an effective vehicle for both validation and vicarious calibration of ocean color satellites. Buoy-mooring platforms are capable of sampling under even the most adverse of weather and sea-state conditions with high temporal resolution for months at a time before the optical sensors and system require servicing (Clark *et al*., 1997; Dickey *et al*., 2001, 2006). On the other hand, ocean color satellites are effectively restricted during even the slightest cloud coverage and wind generated white-cap conditions. Multi-year deployments with periodic recoveries and re-deployments of buoy-mooring systems fitted with optical instrumentation (hereafter referred to as *optical moorings*) have become possible and successful as a result of technological advances in hardware, power sources, data storage, telemetry capabilities, and copper anti-fouling devices (Chavez *et al*., 2000; Manov *et al*., 2004).

Optical moorings have formed the foundation of several long-term ocean monitoring projects and validation and/or vicarious calibration efforts (Chavez *et al*., 1997; Clark *et al*., 1997, 2003; Ishizaka *et al*., 1997; Kishino *et al*., 1997; Dickey *et al*., 1998, 2001, 2006; Letelier *et al*., 2000; Barnes *et al*., 2001; Strutton *et al*., 2001; Pinkerton *et al*., 2003; Spada *et al*., 2007). Moorings-of-opportunity can provide comprehensive, interdisciplinary *in situ* observations complementing satellite remotely sensed data for deriving synergistic descriptions of oceanographic features and their evolution in space and time, as well as providing optical validation and, potentially, vicarious calibration data. Optical moorings have helped facilitate ocean color satellite validation efforts by providing high frequency, ground-truth measurements in a variety of open ocean locations; they have already collectively influenced correction techniques and algorithm development.

Although the potential of optical moorings has been demonstrated, intercomparisons between different measurement and methodological techniques have yet to be standardized. For example, protocols to calculate relevant *in situ* water-leaving radiance, $L_w(\lambda)$, and normalized water-leaving radiance, $L_{wn}(\lambda)$, have been recommended, but detailed descriptions of instrumentation placement, sampling frequency, site-specific limitations, etc. have yet to be standardized and are thus inconsistent between studies (Kuwahara *et al*., 2003). In order to assure that radiometric and bio-optical data acquired from optical moorings meet standards of quality and accuracy, clear and well-documented sampling and data processing methods need to be standardized.

The purpose of this study is to make recommendations for the design and application of optical moorings-of-opportunity for ocean color satellite ground-truthing purposes on a global scale. Specifically, we: (1) demonstrate that moorings-of-opportunity are viable platforms for ocean color satellite validation by comparing *in situ* optical mooring and satellite ocean color match-ups of $L_w(\lambda)$, (2) discuss the quality control and data analysis protocols necessary for quality measurements, and (3) examine different ways to optimally deploy instrumentation to minimize errors.

2. Materials and Procedures

Data relevant to this study were collected on the BTM, which was designed and configured to provide high frequency *in situ* measurements at a fixed location in deep waters off Bermuda for oceanographic science (Dickey *et al*., 2001). The BTM is located at roughly 31°N, 64°W, about 80 km southeast of Bermuda in waters of ~4567 m depth. BTM instrumentation of primary interest to the present study includes a chlorophyll fluorometer at 35 m and radiometers for upwelling radiance and downwelling irradiance. Each of the latter systems, co-located at 14 and 21 m depths, utilize Satlantic, Inc. OCI-200 and OCR-200 radiometers that measure downwelling irradiance, $E_d(\lambda, z)$, and nadir upwelling radiance, $L_u(\lambda, z)$, at seven wavelengths centered at 412, 443, 490, 510, 555, 665, and 683 nm (spectral bandwidth is 10 nm). These wavelengths are compatible with those of the SeaWiFS ocean color imager plus 683 nm. In addition to the subsurface radiometer packages, an OCI-200 was mounted on the BTM surface buoy just above the sea surface for $E_d(\lambda, 0^+)$ and a Satlantic, Inc. Stordat-7 radiometer was deployed at 5 m depth to measure $L_u(\lambda, 5m)$ at the same seven wavelengths as those listed above. Sampling by the OCI/OCR-200 radiometers was done for 45 seconds at 6 Hz every hour. The sampling rate for the Stordat-7 was 2 Hz every hour for 30 seconds. All sensors were factory calibrated following the standards set down by the ocean color community (Mueller and Austin, 2003). Although pre- and post-calibrations of all radiometers were conducted, we utilized the post-calibration for the present study since calibration drift was minimal for all instruments at all wavelengths (<1.5%). The data presented here were collected during the 12th deployment of the BTM, between 30 July and 5 November 1999.

2.1 Data quality assurance/quality control (QA/QC)

A data pre-processing routine was developed to select BTM data deemed appropriate for analysis. This routine involved calculation of the calibrated measurements for the entire deployment at each wavelength for each instrument at each depth and a series of quality assurance and quality control (QA/QC) analyses, described here (Fig. 1A).

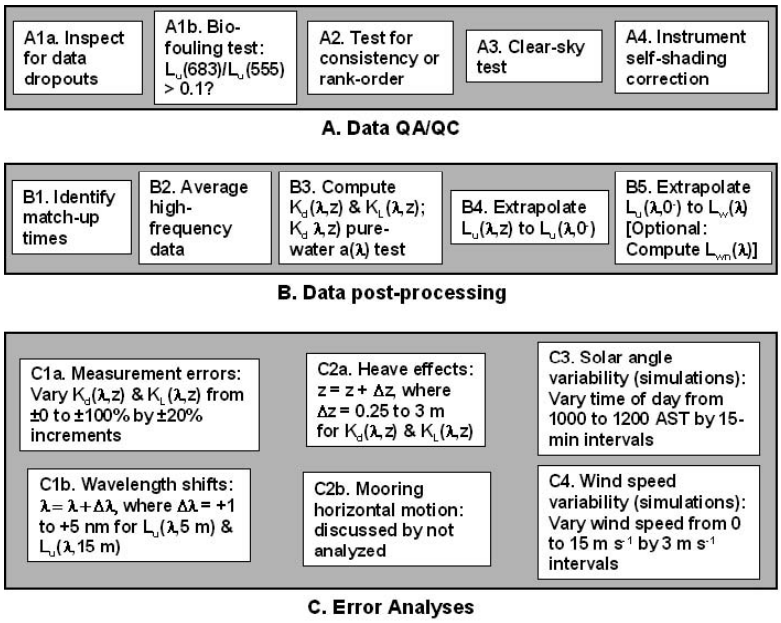

Fig. 1. Flow-chart showing the procedures used during this study: data quality assurance/quality control (QA/QC), post-processing, and error analyses.

(1) The time-series data were inspected and scrutinized for obvious data dropouts from instrument/power failure and symptoms of salt or other depositions on the optical windows of the radiometers. Subsurface radiometric data were subjected to the test for fouling following work by Abbott and Letelier (1998), who suggested that data are affected by bio-fouling when the upwelling radiance ratio of 683/555 nm exceeds 0.1, which is a value appropriate for clear oligotrophic water masses such as those found near Bermuda. In the present study, ratio values for each depth (5, 15, and 21 m) were well below the 0.1 threshold level, suggesting negligible influence from bio-fouling and effectiveness of precautionary anti-fouling methods (i.e. copper shutters; Manov *et al.*, 2004). No data points showed signs of obvious instrument degradation or failure.

(2) The time-series of normalized spectra and wavelength-to-wavelength ratios from each surface and subsurface data set were analyzed to determine the consistency and shape of each spectrum. The purpose of this exercise is to determine whether the wavelength-to-wavelength ratio maintains consistency or "rank-order" throughout the deployment as defined by the relative magnitude of normalized irradiance at all wavelengths, and to determine whether the wavelength-to-wavelength ratio values fall within limits defined by clear-sky models of incident daylight (Kuwahara *et al.*, 2003). It is expected that the collected data should maintain a consistent normalized rank-order unless the instrument sensor is damaged or improperly calibrated. The results obtained from the time series of interest indicate that consistent wavelength-to-wavelength order was maintained; this implies that sensor diode integrity and reliable pre- and post-deployment calibration prevailed.

(3) For incident spectral irradiance above the sea surface, $E_d(\lambda, 0^+)$, a comparison of the magnitudes of measured $E_d(\lambda, 0^+)$ with clear-sky model $E_d(\lambda, \text{clear-sky})$ estimates by Frouin *et al.* (1989) were calculated for the solar zenith angle at each measurement time for the entire deployment. Data were labeled as suspect if the incident measurements exceeded a threshold factor of $1.25 \times E_d(\lambda, \text{clear-sky})$. The factor 1.25 allows measured spectral irradiances to moderately exceed calculated clear-sky irradiances due to scattering from clouds. None of the daily average $E_d(\lambda, 0^+)$ values failed this clear-sky quality control test.

(4) Self-shading by the radiometers was corrected following the methods presented by Gordon and Ding (1992). The error associated with radiometer self-shading, $\varepsilon(\lambda)$, can be represented as:

$$\varepsilon(\lambda) = [L_u^T(\lambda) - L_u^M(\lambda)]/L_u^T(\lambda), \quad (1)$$

and

$$\varepsilon(\lambda) = 1 - \exp[-k\, a_t(\lambda) r], \quad (2)$$

where $L_u^T(\lambda)$ is radiance corrected for self-shading and

$L_u^M(\lambda)$ is uncorrected radiance, $a_t(\lambda)$ is the total absorption coefficient, r is the radius of the instrument housing (r = 0.44 m), and k = 2/tanθ_{0w} (θ_{0w} is the refracted solar zenith angle). This method assumes that absorption dominates over scattering processes, which is true for Sargasso Sea waters. The absorption coefficient was estimated using the model presented by Morel (1991):

$$a_t(\lambda) = [a_w(\lambda) + 0.06a_{chl}^*(\lambda)Chl^{0.65}][1 + 0.2y(\lambda)], \quad (3a)$$

where

$$y(\lambda) = \exp[-0.014(\lambda - 440)], \quad (3b)$$

$a_w(\lambda)$ is the absorption coefficient of pure water (Pope and Fry, 1997), $a_{chl}^*(\lambda)$ is the chlorophyll-specific absorption coefficient (Prieur and Sathyendranath, 1981), and Chl is the BTM-measured chlorophyll-*a* concentration. Because values of $a_t(\lambda)$ are extremely low in the Sargasso Sea, radiometer self-shading effects were small, with $\varepsilon(\lambda) \approx 1\%$. We assumed that buoy-shading effects were negligible; radiometers were mounted well below the base of the buoy ($z \geq 5$ m) and on an arm extending away from the centerline of the mooring. In addition, satellite and mooring match-up times used in this study were all within two hours of Bermuda local noon, reducing the effects of the buoy shading.

2.2 Data post-processing

After performing the QA/QC protocols for moored radiometric data, SeaWiFS and mooring data match-up times were identified. Successful match-ups are most dependent on clear sky conditions and equivalent spatial coverage (i.e. mooring occurring in a pixel). Of the entire 101-day BTM radiometric time series between 30 July and 5 November 1999, 23 suitable SeaWiFS satellite match-ups were available, or roughly 23% of collected data. For comparison, PlyMBODy optical data, collected in a relatively cloudy oceanic region (English Channel), matched up less than 6% of the time during a ~10 month deployment and about 10% of MOBY data are realized for SeaWiFS match-ups (Pinkerton *et al*., 2003). These differences underscore both the limitations and benefits of using optical moorings-of-opportunity for satellite validation and vicarious calibration, as moorings provide autonomously collected, long, continuous time series from which satellite match-up data may be selected.

For the purpose of ocean color satellite validation it is necessary to average individual high-frequency measurements. The averaging of high frequency data accounts for fluctuations in the incident light field, such as those caused naturally by wave-focusing (e.g., Zaneveld *et al*., 2001; Zheng *et al*., 2002), and allows comparisons to be made with satellites using a single, averaged measurement for a particular satellite image. For the BTM data sets, three different averaging techniques were tested. For each wavelength at each depth: (1) daily averages were calculated using high-frequency data from 0700 to 1900 Atlantic Standard Time (AST), (2) averages were computed for daily noon between 1000 and 1400 AST, and (3) 1-hr averages were computed, centered around the time nearest to the SeaWiFS satellite overpass times. Satellite overpass times were all within 1-hr of mooring data collection.

The vertical diffuse attenuation coefficients for downwelling irradiance and upwelling radiance, $K_d(\lambda, z)$ and $K_L(\lambda, z)$, respectively, were determined directly from QA/QC'ed radiometric measurements. Given downwelling irradiance measured by radiometers at two different depths, the diffuse attenuation coefficient for downwelling irradiance at the midpoint of the two depths is given by:

$$K_d(\lambda, z) = -\frac{d}{dz}\left[\ln E_d(\lambda, z)\right], \quad (4a)$$

$$= -\frac{1}{\Delta z}\ln\frac{E_d(\lambda, z_2)}{E_d(\lambda, z_1)}, \quad (4b)$$

where depths $z_2 > z_1$. $K_d(\lambda, 18m)$ was computed using measured $E_d(\lambda, z)$ at 15 and 21 m. Further QA/QC analyses are performed on calculated $K_d(\lambda, z)$; $K_d(\lambda, z)$ should be greater than the absorption coefficient of pure water at each wavelength (Pope and Fry, 1997). Throughout the time series, $K_d(\lambda, 18m)$ values for λ = 665 and 683 nm failed the pure water absorption coefficient test, likely due to the low signal-to-noise ratio for $E_d(\lambda, z)$ at the red wavelengths. Similar to $K_d(\lambda, z)$, given two underwater upwelling radiance sensors, the vertical attenuation coefficient for upwelling radiance at the center of that depth interval is calculated by:

$$K_L(\lambda, z) = -\frac{d}{dz}\left[\ln L_u(\lambda, z)\right], \quad (5a)$$

$$= -\frac{1}{\Delta z}\ln\frac{L_u(\lambda, z_2)}{L_u(\lambda, z_1)}. \quad (5b)$$

$K_L(\lambda, 10m)$ was computed from measurements of $L_u(\lambda, 5m)$ and $L_u(\lambda, 15m)$, whereas $K_L(\lambda, 18m)$ was obtained using $L_u(\lambda, z)$ measurements at 15 and 21 m, and finally $K_L(\lambda, 13m)$ was calculated from $L_u(\lambda, 5m)$ and $L_u(\lambda, 21m)$.

Water leaving radiance, $L_w(\lambda)$, was determined by extrapolating upwelling radiance measured at depth z to the surface following:

Table 1. Comparisons of $L_u(\lambda, 0^-)$ calculated using Eq. (6a) and vertical diffuse attenuation coefficients for upwelling radiance and downwelling irradiance computed at and extrapolated from various depths. Each table cell shows results at three wavelengths: 412, 490, and 555 nm, respectively computed using averages between 0700 and 1900 AST. Percentage differences were calculated using Eq. (7) and averaged over the time series. Differences of less than 10% are indicated in bold.

$L_u(\lambda,0^-)$ extrapolated using:	$L_u(\lambda,0^-)$ extrapolated using:					
	K_d(18m) L_u(5m)	K_d(18m) L_u(15m)	K_d(18m) L_u(21m)	K_L(10m) L_u(5m)	K_L(18m) L_u(15m)	K_L(13m) L_u(21m)
K_d(18m) L_u(5m)		**6.7%**	15%	**–3.3%**	–13%	**–4.6%**
	—	**–6.3%**	**0.16%**	**3.2%**	–23%	**–0.05%**
		–37%	–32%	19%	–51%	**10%**
K_d(18m) L_u(15m)	**–6.7%**		**7.9%**	**–10%**	–20%	–11%
	6.3%	—	**6.5%**	**9.5%**	–16%	**6.3%**
	37%		**5.7%**	55%	–14%	47%
K_d(18m) L_u(21m)	–15%	**–7.9%**		–18%	–28%	–19%
	–0.16%	**–6.5%**	—	**3.0%**	–23%	**–0.21%**
	32%	**–5.7%**		50%	–20%	41%
K_L(10m) L_u(5m)	**3.3%**	**10%**	18%		**–9.8%**	**–1.2%**
	–3.2%	**–9.5%**	**–3.0%**	—	–26%	**–3.2%**
	–19%	–55%	–50%		–57%	**–8.8%**
K_L(18m) L_u(15m)	13%	20%	28%	**9.8%**		**8.6%**
	23%	16%	23%	26%	—	22%
	51%	14%	20%	57%		60%
K_L(13m) L_u(21m)	**4.6%**	11%	19%	**1.2%**	**–8.6%**	
	0.05%	**–6.3%**	**0.21%**	**3.2%**	–22%	—
	–10%	–47%	–41%	**8.8%**	–60%	

$$L_u\left(\lambda, 0^-\right) = L_u\left(\lambda, z\right) e^{K_L(\lambda,z)z}, \qquad (6a)$$

and through the surface according to:

$$L_w(\lambda) = 0.543 L_u(\lambda, 0^-), \qquad (6b)$$

where only nadir-viewing geometry is considered (the surface reflectance becomes independent of wind speed) and the constant value, 0.543, corresponds to the upward transmittance term (Austin, 1974). $L_u(\lambda, 0^-)$ and $L_w(\lambda)$ were computed 12 different ways using Eqs. (6a) and (6b): (1)–(3) $K_L(\lambda, 10m)$ and $L_u(\lambda, z)$, (4)–(6) $K_L(\lambda, 13m)$ and $L_u(\lambda, z)$, and (7)–(9) $K_L(\lambda, 18m)$ and $L_u(\lambda, z)$, where z = 5, 15, and 21 m; $K_d(\lambda, 18m)$ was substituted for $K_L(\lambda, z)$ and (10) $L_u(\lambda, 5m)$, (11) $L_u(\lambda, 15m)$, and (12) $L_u(\lambda, 21m)$. For this study we present $L_w(\lambda)$ rather than normalized water-leaving radiance, $L_{wn}(\lambda)$, in order to evaluate effects of solar zenith angle variability.

2.3 SeaWiFS data processing

SeaWiFS data were provided by the NASA SIMBIOS (National Aeronautics and Space Administration Sensor Intercomparison for Marine Biological and Interdisciplinary Ocean Studies) project for a 5×5 pixel box (roughly 25 sq. km) centered on the nominal BTM location. The 5×5 pixel box was selected as opposed to a 1×1 pixel box to maximize satellite mach-ups due to environmental variability at the BTM site and to provide more robust data. A total of 1,251 SeaWiFS files (global and site-specific local area coverage) were processed; 246 of these files passed to Level 2 SeaWiFS products and were considered useable. After reducing data points to those that had at least one valid pixel in the 5×5 box, 87 match-ups remained. Of these 87 total match-ups, 46 local area coverage data points remained once the redundant data from global area coverage were removed. Twenty-three of these data points matched-up with the BTM data collection period and were used for the comparative analysis with the BTM radiometer data. Due to frequent failure of the pure water absorption coefficient test, the red wavelengths of 665 and 683 nm were not used in the analyses presented here.

3. Assessment and Results

In the present study, downwelling irradiance and upwelling radiance were measured on a mooring at multiple depths, allowing us to establish the requirements for

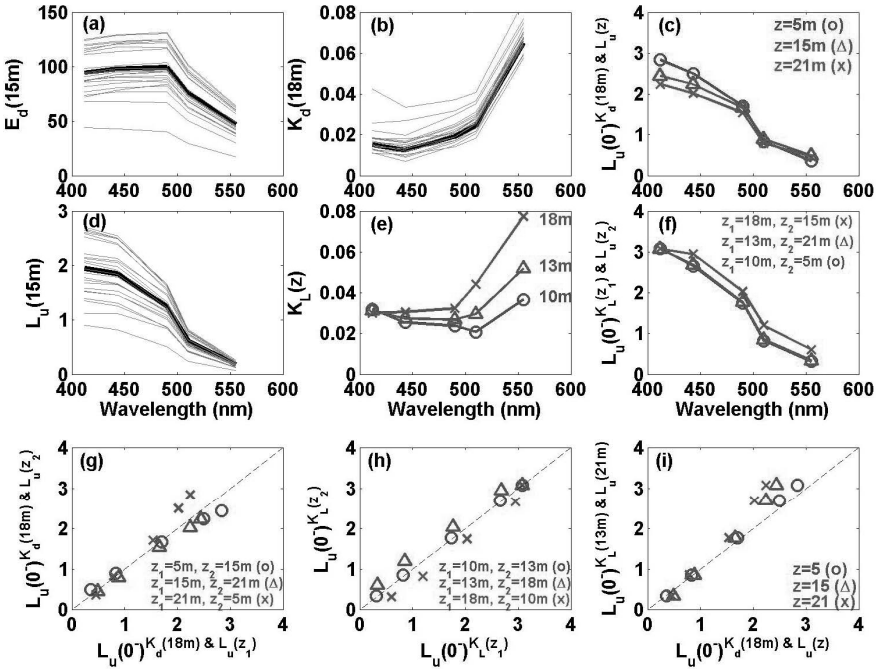

Fig. 2. Mean spectra averaged over the time series (n = 23; all spectra shown in grey) of: (a) BTM-measured $E_d(\lambda, 15m)$; (b) $K_d(\lambda, 18m)$ computed using Eqs. (4a) and (4b); (c) $L_u(\lambda, 0^-)$ extrapolated using $K_d(\lambda, 18m)$ and $L_u(\lambda, z)$ (Eq. (6a)); (d) BTM-measured $L_u(\lambda, 15m)$; (e) $K_L(\lambda, z)$ computed using Eqs. (5a) and (5b); (f) $L_u(\lambda, 0^-)$ extrapolated using $K_L(\lambda, z_1)$ and $L_u(\lambda, z_2)$ (Eq. (6a)). Comparisons between $L_u(\lambda, 0^-)$ extrapolated using (g) $K_d(\lambda, 18m)$ and $L_u(\lambda, z_1)$ vs. $L_u(\lambda, z_2)$; (h) $K_L(\lambda, z_1)$ versus $K_L(\lambda, z_2)$ and $L_u(\lambda, z)$ as in Table 1; (i) $K_d(\lambda, 18m)$ and $L_u(\lambda, z)$ versus $K_L(\lambda, 13m)$ and $L_u(\lambda, 21m)$. Wavelength notations in figure are suppressed.

reliable measurements necessary for validation of ocean color satellite data.

3.1 Vertical diffuse attenuation coefficients, $K_d(\lambda, z)$ and $K_L(\lambda, z)$

The vertical diffuse attenuation coefficients for upwelling radiance and downwelling irradiance, $K_L(\lambda, z)$ and $K_d(\lambda, z)$, evaluated for multiple depths were used to extrapolate $L_u(\lambda, 0^-)$ (Fig. 3). Comparisons were made between derived values of $L_u(\lambda, 0^-)$ (Table 1) to determine the optimal placement of radiometers for satellite validation purposes. Percentage differences were computed using the following equation:

$$\%\mathrm{diff}(\lambda) = 100 \times \left[\frac{\left[L_u(\lambda, 0^-)_1 - L_u(\lambda, 0^-)_2 \right]}{0.5\left[L_u(\lambda, 0^-)_1 - L_u(\lambda, 0^-)_2 \right]} \right], \quad (7)$$

where the subscripts 1 and 2 specify two different methods of computing $L_u(\lambda, 0^-)$, e.g., 1: using $K_L(\lambda, 10m)$ and $L_u(\lambda, 5m)$ and 2: using $K_d(\lambda, 18m)$ and $L_u(\lambda, 5m)$. Note that these comparisons involved mooring measurements only. In general, derivations of $L_u(\lambda, 0^-)$ using $K_d(\lambda, 18m)$ with $L_u(\lambda, 5m)$, $L_u(\lambda, 15m)$, and $L_u(\lambda, 21m)$ (Eq. (6a)) were comparable with average percentage differences of near 10% for all wavelengths except 555 nm (Table 1; Fig. 2). As expected, larger deviations were found when comparing vertical diffuse attenuation coefficients using 5 m extrapolated to 21 m. Also as expected, for derivations of $L_u(\lambda, 0^-)$ using $K_L(\lambda, z)$ with $L_u(\lambda, 5m; 15m; 21m)$ at different depths, differences were less than 1% when comparing extrapolations from the same depths used in the computation of $K_L(\lambda, z)$ and on the order of 10% for extrapolations from the other two depths (data not shown). For example, $L_u(\lambda, 0^-)$ computed using $K_L(\lambda, 10m)$ and $L_u(\lambda, 5m)$ was comparable to $L_u(\lambda, 0^-)$ computed using $K_L(\lambda, 10m)$ and $L_u(\lambda, 15m)$ because $K_L(\lambda, 10m)$ was derived from measurements of $L_u(\lambda, 5m)$ and $L_u(\lambda, 15m)$.

Comparisons between $L_u(\lambda, 0^-)$ derived using $K_L(\lambda, z)$, where z = 10, 13, or 18 m, varied depending on the extrapolation depth. Lowest percentage differences were found for $L_u(\lambda, 0^-)$ derived using $K_L(\lambda, 10m)$ and $K_L(\lambda, 13m)$, i.e. using the two uppermost radiometers and the upper and lowest mounted radiometer (Table 1). The largest deviations were found for computations using $K_L(\lambda, 18m)$, illustrating that optical properties between 15 and 21 m were different from those properties between

Table 2. Comparisons between SeaWiFS-measured and mooring-derived values of $L_w(\lambda)$. Each table cell shows three different averaging schemes: daily averaged (0700–1900 AST), 4-hr averaged (1000–1400 AST), and 1-hr averaged (nearest satellite overpass time) differences, respectively. Percentage differences were computed using Eq. (8) and averaged over the time series.

SeaWiFS-measured:	$L_w(\lambda)$ derived using mooring:					
	K_d(18m) L_u(5m)	K_d(18m) L_u(15m)	K_d(18m) L_u(21m)	K_L(10m) L_u(5m)	K_L(18m) L_u(15m)	K_L(13m) L_u(21m)
L_w(412 nm)	–56%	–59%	–62%	–54%	–49%	–54%
	–30%	–37%	–42%	–25%	–22%	–25%
	–23%	–34%	–40%	–17%	–17%	–17%
L_w(443 nm)	–60%	–61%	–65%	–60%	–50%	–59%
	–37%	–41%	–47%	–35%	–24%	–34%
	–32%	–39%	–45%	–27%	–20%	–27%
L_w(490 nm)	–57%	–54%	–57%	–58%	–46%	–57%
	–32%	–31%	–35%	–32%	–17%	–30%
	–26%	–28%	–34%	–24%	–12%	–23%
L_w(510 nm)	–64%	–58%	–52%	–66%	–45%	–64%
	–42%	–36%	–43%	–45%	–16%	–42%
	–38%	–34%	–41%	–38%	–11%	–36%
L_w(555 nm)	–61%	–43%	–47%	–68%	–34%	–65%
	–38%	–13%	–18%	–47%	3.8%	–42%
	–33%	–9.6%	–16%	–41%	11%	–37%

5 and 15 m. $L_u(\lambda, 0^-)$ derived using $K_d(\lambda, z)$ versus those using $K_L(\lambda, z)$ were comparable, except for $K_L(\lambda, 18m)$ (Table 1; Fig. 2). In general, differences computed at 555 nm were greater than those at the other wavelengths. Radiance spectra were at a minimum at this wavelength; low signal-to-noise ratios in clear Sargasso Sea waters may have been the reason for poor correlations at 555 nm (Fig. 2). Daily averaged (over daylight hours), 4-hr averaged (centered at noon), and 1-hr averaged (centered at overpass) results were quite similar to each other.

BTM data showed that $K_d(\lambda, z)$ was reliable in propagating $L_u(\lambda, z)$ measurements at depth to just below the surface. Because $K_d(\lambda, z)$ undergoes a quality control screening (pure water absorption coefficient comparison) and it is an important variable in many bio-optical models (e.g., Morel and Maritorena, 2001), it may be useful in some operations to utilize $K_d(\lambda, z)$ to extrapolate $L_u(\lambda, z)$ to the surface only, when $K_L(\lambda, z)$ is not readily available. In other words, if a limited number of radiometers can be deployed or if some sensors fail, it may be desirable to utilize one $L_u(\lambda, z)$ sensor and two $E_d(\lambda, z)$ sensors. Regardless of whether $K_d(\lambda, z)$ or $K_L(\lambda, z)$ is (or both are) used, sensors deployed at multiple depths are strongly recommended to assure against data loss in the event of sensor failure.

3.2 Water-leaving radiance

Water-leaving radiances were computed using all derived $L_u(\lambda, 0^-)$ quantities and Eq. (6b) (12 different computations). These mooring-derived values were then compared to SeaWiFS-measured $L_w(\lambda)$ (Fig. 3; Table 2). Percentage differences were computed according to the following equation:

$$\%\text{diff}(\lambda) = 100 \times [(L_w(\lambda)_2 - L_w(\lambda)_1)/L_w(\lambda)_1], \quad (8)$$

where $L_w(\lambda)_2$ and $L_w(\lambda)_1$ are water-leaving radiances measured by SeaWiFS and derived from BTM radiometric measurements, respectively. Comparisons between satellite-and mooring-derived $L_w(\lambda)$ were wavelength dependent. For the uppermost water column (5–15 m), percentage differences generally increased with wavelength. Interestingly, the opposite was true for $L_w(\lambda)$ derived from $L_u(\lambda, 21m)$. The reason for this is unknown. Pinkerton *et al*. (2003) reported higher absolute percentage differences between SeaWiFS-measured and PlyMBODy-derived $L_{wn}(\lambda)$ at the blue (412–443 nm) and red (670 nm) wavelengths (56 and 77%) compared to the blue-green to green wavebands (490–555 nm = ~20%), likely due to increased turbidity in the region.

BTM results showed that mooring data averaged over

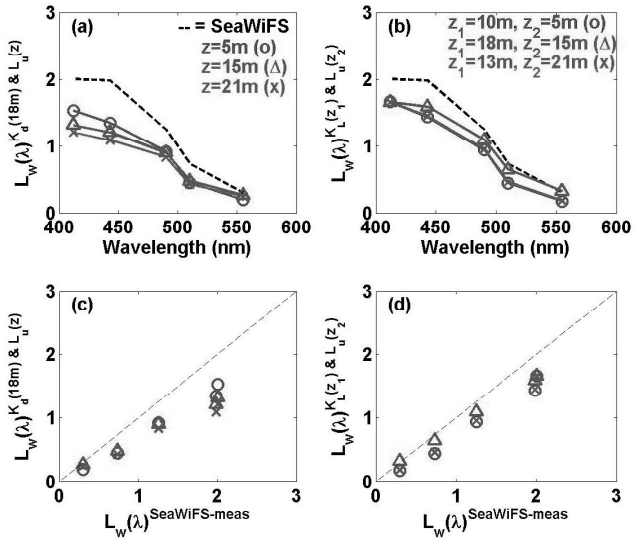

Fig. 3. Time-averaged water-leaving radiance, $L_w(\lambda)$, spectra (n = 23) measured by SeaWiFS and derived (a) using $K_d(\lambda, 18m)$ and $L_u(\lambda, z)$; (b) using $K_L(\lambda, z_1)$ and $L_u(\lambda, z_2)$. Comparisons between $L_w(\lambda)$ (c) derived using the three different depths in (a); and (d) derived using the three different depth combinations in (b).

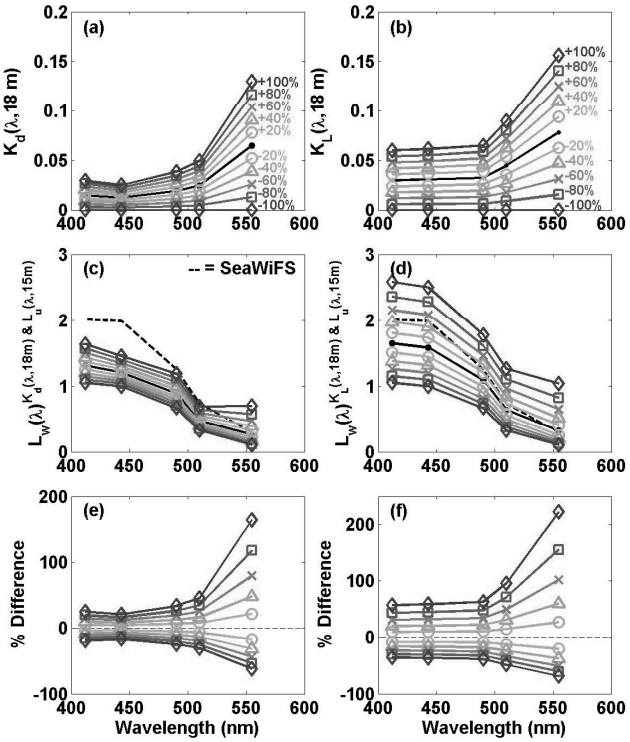

Fig. 4. $K_d(\lambda, 18m)$ and $K_L(\lambda, 18m)$ error analysis results. (a) $K_d(\lambda, 18m)$ averaged over the time series (n = 23; black line with closed circles) plotted with $K_d(\lambda, 18m) \pm K_d(\lambda, 18m) \times 20\%$, 40%, 60%, 80%, and 100%. (b) As in (a) but for $K_L(\lambda, 18m)$. (c) and (d) Derived $L_w(\lambda)$ using vertical diffuse attenuation coefficients in (a) and (b), respectively, and Eqs. (6a) and (6b). (e) and (f) Percent differences in $L_w(\lambda)$ (Eq. (8)).

daylight hours (0700–1900 AST) did not compare well with ocean color satellite measurements, which are collected at one instant in time. Absolute differences were of the order of 50–70% for all wavelengths at all depths using $K_L(\lambda, z)$ or $K_d(\lambda, 18m)$. On the other hand, results for averaging performed over 4-hrs and 1-hr were improved as indicated by absolute differences of roughly 25% (30–40%) and <20% (20–40%), respectively for $L_w(\lambda)$ derived using $K_L(412$ nm, z) [$K_d(412$ nm, 18 m)] (Fig. 3; Table 2). In all three time averaging cases, derivations using $K_L(\lambda, 18m)$ with $L_u(\lambda, 15$ and 21m) were better than those for $K_L(\lambda, 10m)$, $K_L(\lambda, 13m)$, or $K_d(\lambda, 18m)$. Recall that results from vertical diffuse attenuation coefficient comparisons showed that optical properties between 15 and 21 m were different from those properties between 5 and 15 m.

4. Discussion

In general, the differences between satellite-measured and BTM-derived $L_w(\lambda)$ were comparable to those found using other optical moorings, except when averages between 0700–1900 AST were used. Average differences over the SeaWiFS wavebands were 37% for PlyMBODy results (Pinkerton *et al*., 2003). Water-leaving radiance derived using $K_L(\lambda, 18m)$ and $L_u(\lambda, 15m)$ were greatly improved, with differences of 20% in the blue, decreasing to 11% in the green wavebands. Various error analyses associated with *in situ* measurements were conducted to evaluate the impact of: instrumentation inaccuracies (e.g., radiometric drift, miscalibrations, biofouling, wavelength shifts), mooring motion, and environmental effects (solar angle and wind speed) on the discrepancies related to methods of estimating $L_w(\lambda)$ (Fig. 1C). Radiance is an extremely difficult measurement to make. For example, Chang *et al*. (2003) found differences of ~20% between three different *in situ* methods of estimating $L_w(\lambda)$.

4.1 Instrumentation effects

Propagation of errors from inaccurate measurements of $E_d(\lambda, z)$ and $L_u(\lambda, z)$ caused by, e.g., radiometer drift, miscalibration, or biofouling, were investigated by computing $K_d(\lambda, 18m)$ and $K_L(\lambda, 18m)$ from time-averaged BTM measurements of $E_d(\lambda, z)$ and $L_u(\lambda, z)$, where z = 15 and 21, then varying these values of $K_d(\lambda, 18m)$ and $K_L(\lambda, 18m)$ from 0 to ±100% by steps of ±20%. Water-leaving radiance was derived from variable values of $K_d(\lambda, 18m)$ and $K_L(\lambda, 18m)$ and BTM-measured

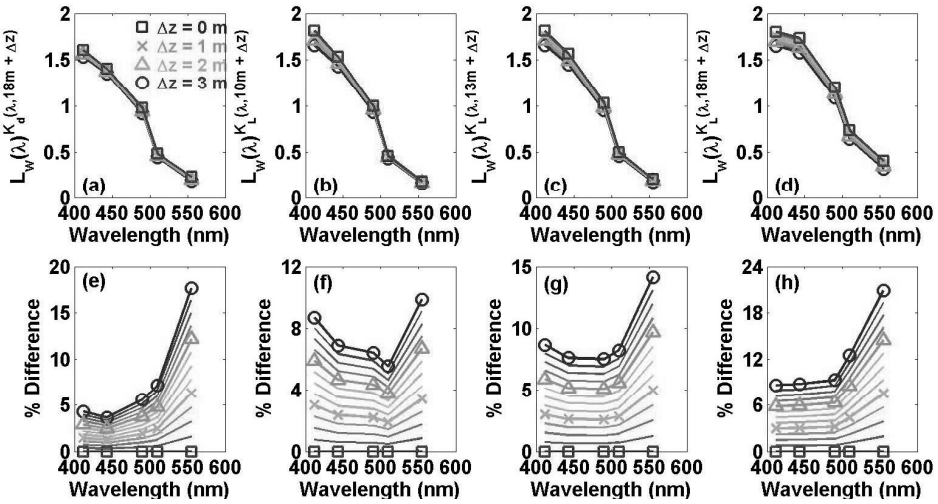

Fig. 5. Results from mooring heave error analysis. $L_w(\lambda)$ spectra extrapolated using averaged (n = 23) (a) $K_d(\lambda, 18m + \Delta z)$ and $L_u(\lambda, 5m + \Delta z)$; (b) $K_L(\lambda, 10m + \Delta z)$ and $L_u(\lambda, 5m + \Delta z)$; (c) $K_L(\lambda, 13m + \Delta z)$ and $L_u(\lambda, 21m + \Delta z)$; and (d) $K_L(\lambda, 18m + \Delta z)$ and $L_u(\lambda, 15m)$, and Δz = 0.25 to 3 m by increments of 0.25 m. Percentage differences in $L_w(\lambda)$ between non-depth-shifted (Δz = 0 m) and depth-shifted parameters (Eq. (8)) (e)–(h) derived using (a)–(d).

$L_u(\lambda, 15m)$ (Eqs. (6a) and (6b)). The results of this analysis are shown in Fig. 4. Naturally, higher values of diffuse attenuation coefficients resulted in greater changes, therefore the computation of $L_w(\lambda)$ using $K_L(\lambda, 18m)$ was much more sensitive to changes than those using $K_d(\lambda, 18m)$, and longer wavelengths were most affected. Moreover, increases as opposed to decreases in $K_d(\lambda, 18m)$ and $K_L(\lambda, 18m)$ resulted in higher percentage differences between derived $L_w(\lambda)$. Generally, a 20% error in the computation of $K_d(\lambda, z)$ and $K_L(\lambda, z)$ resulted in <10% errors in the derivation of $L_w(\lambda)$, however up to 60% errors were found when $K_L(\lambda, z)$ was 100% of its true value (blue wavelengths). These errors increase exponentially with increasing wavelength and would be even greater for Case II water.

Variability in mooring-derived $L_w(\lambda)$ can also be attributed to radiometer wavelength shifts (up to ±5 nm caused by temperature variations). Wavelength shifts of +1 to +5 nm by steps of 1-nm were applied to measured $L_u(\lambda, 5m)$ and $L_u(\lambda, 15m)$. $K_L(\lambda, 10m)$ was then derived following Eqs. (5a) and (5b), and $L_u(\lambda, 0^-)$ and $L_w(\lambda)$ were computed using Eqs. (6a) and (6b), extraolating from $L_u(\lambda, 5m)$. Percentage differences were calculated using Eq. (8), with $L_w(\lambda)_2$ = wavelength-shifted values and $L_w(\lambda)_1$ = non-wavelength-shifted values. Shifts of 1-nm resulted in <2.5% change across all wavelengths (average difference was 1.3%), whereas ~6.5% changes occurred with a 5-nm shift (range of 2.2–13.2%). The blue-green wavelengths (490 and 510 nm) were most sensitive to wavelength shifts (data not shown). Results from shifts of –1 to –5 nm were the same but of opposite sign.

4.2 Mooring motion

Vertical mooring heave effects on radiometric measurements, which are dependent on weather and sea-state conditions, were examined by deriving $L_w(\lambda)$ from $L_u(\lambda, 0^-)$ extrapolated using a range of $K_d(\lambda, z + \Delta z)$ and $K_L(\lambda, z + \Delta z)$ where z = 18 m for $K_d(\lambda, z)$ and z = 5, 15, and 21 m for $K_L(\lambda, z)$, and Δz was varied from 0.25 to 3 m by steps of 0.25 m. Pressure sensors mounted on the BTM have measured the maximum heave of the BTM as about 3 m. Percentage differences were computed using Eq. (8), where $L_w(\lambda)_2$ = depth-shifted values and $L_w(\lambda)_1$ = non-depth-shifted values. The results show that heave effects increased with heave-depth (Δz) and depth of vertical attenuation coefficient, i.e. maximum effects were seen for Δz = 3 m and for derivations using $K_L(\lambda, 18m)$ (Fig. 5). Heave effects were also more prominent at 555 nm than other wavelengths, although differences at 410 nm for $K_L(\lambda, 10m)$ were relatively high. An upward mooring heave of 1-m resulted in differences between depth-shifted and non-depth shifted derivations of L_w(490 nm) ranging between 2.2% (3.4% for 555 nm) for K_L(490 nm, 10 m) to 3.2% (7.5% for 555 nm) for K_L(490 nm, 18 m). Differences of 6.4% (9.8% for 555 nm) and 9.2% (20.9% for 555 nm) were found for L_w(490 nm) with a heave of 3-m (Fig. 5). Heave effects can be corrected by using pressure sensors mounted at the same depth as radiometers.

Mooring horizontal motions related to the watch-circle (i.e. maximum distance a mooring travels around its anchor) have not been analyzed here, but horizontal variability can affect satellite-to-mooring match-ups (Chang and Gould, 2006). Mooring watch-circles are dependent

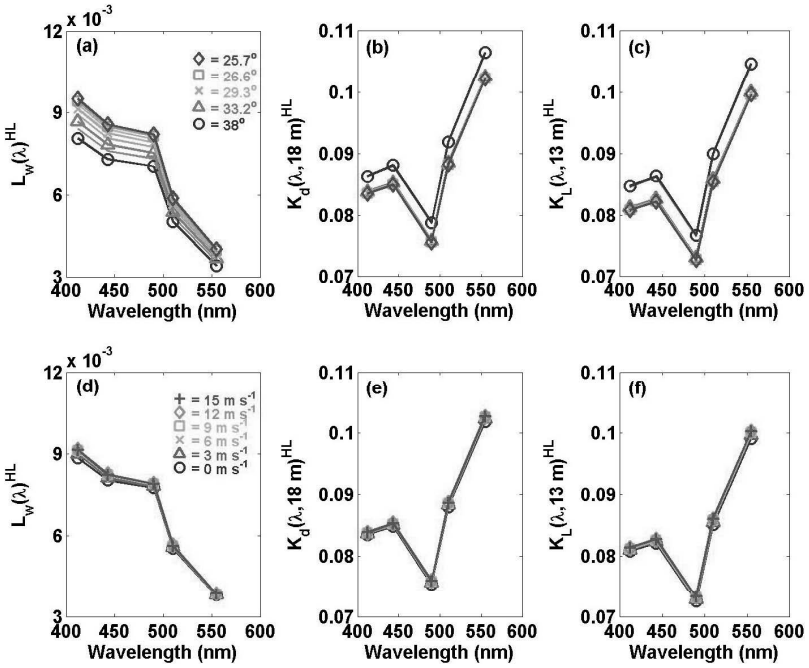

Fig. 6. Results from environmental variability analysis. Simulated $L_w(\lambda)$, $K_d(\lambda, 18m)$ and $K_L(\lambda, 13m)$ computed using input variables described in Discussion: Environmental variability section and: (a)–(c) Variable solar zenith angles for 1000 to 1200 AST, by increments of 15-min (symbols denote every 30-min) and (d)–(f) variable wind speeds.

on water depth, wind speed and direction, currents, sea-state, and type of mooring design (i.e. semi-taught versus catenary). The BTM watch-circle for the semi-taught design is 5 km diameter whereas SeaWiFS and (MODIS-aqua) spatial resolution is ~1 km. Therefore, equivalent spatial coverage of SeaWiFS and mooring data may not be obtained when matching the latitude and longitude of the mooring's anchor with a satellite pixel. This does not pose a serious problem under horizontally homogeneous atmospheric and oceanic conditions, but may greatly affect match-ups in spatially variable environments (i.e. coastal ocean as described by Chang and Gould, 2006). Latitude and longitude obtained from a surface-mounted global positioning system (GPS) can help alleviate issues associated with mooring horizontal motions.

4.3 Environmental variability

Mismatches between satellite-measured and mooring-derived $L_w(\lambda)$ can also be attributed to environmental conditions such as solar angle variability due to mismatched satellite overpass times and variable wind speeds, which are related to transmission across the air-sea interface (Eq. (6b)). These factors were evaluated using the radiative transfer model, Hydrolight. Briefly, the well-documented Hydrolight model solves radiative transfer equations in water, based on invariant imbedding theory (Mobley, 1994). Hydrolight output data relevant to this study include $K_d(\lambda, z)$, $K_L(\lambda, z)$ at z = 10, 13, and 18 m, and $L_w(\lambda)$. Necessary inputs to Hydrolight include the boundary conditions and the inherent optical properties (IOPs). The IOPs were obtained from a historical Case I water model, assuming two components: pure water and chlorophyll-bearing particles with co-varying colored dissolved organic matter and detritus. Pure water coefficients were taken from Pope and Fry (1997). Chlorophyll concentration (Chl) was assumed to be constant with depth; Chl = 0.515 μg l^{-1}, which was the average Chl measured by the BTM over the period of interest. Hydrolight input boundary conditions include wind speed, solar angle, cloud cover, downwelling sky irradiance, and ocean bottom type. Cloud cover was held at 0%, downwelling sky irradiance was computed directly from the RADTRAN model and waters were assumed to be optically deep (i.e. no influences from the ocean bottom). Two different simulations were run with these inputs:

(1) Wind speed was held constant at 5 m s^{-1} while solar angle was varied from 38.0 to 25.7°. The angles were obtained by calculation of solar zenith angle between 1000 and 1200 AST by steps of 15-min. In addition to the sampling time of day, these computations required latitude and Julian day (JD; equations (2-2) and (2-3) from Kirk, 1994). The latitude of the BTM is 31.7311°N and JD was set at the approximate midpoint of the time series of interest, JD = 250 (7 September 1999). Differences were

evaluated between each solar angle and 25.7° (noontime solar zenith angle), e.g., 25.7 compared to 38.0°, 25.7 and 35.5°, etc. Solar angle had a great impact on computations of $L_w(\lambda)$, as indicated above. A 2-hr (1-hr) difference in time resulted in ~15% (~4%) differences in derived $L_w(\lambda)$. Lower wavelengths were slightly more affected by increasing solar angles (Fig. 6). Values of $K_d(\lambda, z)$ and $K_L(\lambda, z)$ remained relatively unchanged (differences of <1%) until solar angle increased to more than 7.5° from solar noon or >1.5 hours from 1200 AST. Differences then increased to 5–6%. These errors associated with solar zenith angle variability have been reduced significantly with the computation of $L_{wn}(\lambda)$.

(2) Wind speed was varied from 0 to 15 m s^{-1} by steps of 3 m s^{-1} while solar angle was held constant at 30°. All other inputs were the same as for simulation (1). Differences reported were calculated between 0 m s^{-1} and each increment of increasing wind speed, e.g., 0 and 3 m s^{-1}, 0 and 9 m s^{-1}, etc. It was found that wind effects were minimal, with less than 3.5% difference between $L_w(\lambda)$ computed for 0 m s^{-1} and 15 m s^{-1} wind speeds. Effects decreased with increasing wavelengths (Fig. 6). The influence of wind speeds on $K_d(\lambda, z)$ and $K_L(\lambda, z)$ were similarly small (<2.2%) but increased with increasing wavelength (Fig. 6).

5. Recommendations and Conclusions

Our recommendations for the use of moorings-of-opportunity for ocean color satellite validation (oligotrophic waters) are as follows:

- Comparisons between the pre- and post-radiometer calibrations are essential (Mueller and Austin, 2003). It was confirmed that stringent comparisons between the two are necessary to verify how radiometer diodes might drift during deployment.
- Proper anti-biofouling precautions and procedures are essential for successful data collection. In addition to shutters, wipers and anti-fouling material, we recommend that time-series data should be inspected for potential fouling signals.
- QA/QC methods, e.g., clear-sky model and pure-water comparisons, must be employed and their usability has been confirmed.
- Although instrument self-shading effects are relatively small in clear, oceanic waters, correction factors are relatively simple to compute and should be used as confirmed in the present study.
- One-hour averages of high resolution time series measurements of $E_d(\lambda, z)$ and $L_u(\lambda, z)$ centered nearest to the satellite overpass time showed the best results compared to other time-averaging methods, but 4-hr averages around daily noon are also suitable. Averaging helps alleviate problems associated with wave focusing, intermittent cloud cover and other environmental variability at site.
- Extrapolations of $L_u(\lambda, z)$ to $L_w(\lambda)$ are more accurate when $K_L(\lambda, z)$ is used, as confirmed in the present study. However, $K_d(\lambda, z)$ can be a reasonable alternative extrapolation variable. Here it is important to clarify that although $K_d(\lambda, z)$ and $K_L(\lambda, z)$ are completely different optical properties, in some instances when instruments fail and/or only instrument deployments are possible an alternative option may be utilized.
- Pressure sensors should be co-located with radiometers to enable corrections due to mooring heave and instrumentation effects, i.e. radiometer wavelength shifts must be considered.
- A surface buoy-mounted GPS is necessary for accurate mooring-to-satellite pixel match-ups in horizontally variable environments.
- Radiometers should be placed within one optical depth of the sea surface, above the subsurface chlorophyll maximum, but also at a depth below the influence of buoy shadowing effects. Procedures to address potential buoy shadow effects are necessary.
- At least two upwelling radiance and two downwelling irradiance sensors, i.e. sensor redundancy, are recommended in the case of sensor failure.

While dedicated calibration buoys such as the MOBY, YBOM and BOUSSOLE systems contribute to direct satellite vicarious calibration efforts, we show that moorings-of-opportunity can be cost-effective methods for validating data collected by ocean color satellites when using careful quality control procedures. Time-averaged percentage differences between SeaWiFS-measured and BTM mooring-derived $L_w(\lambda)$ were about 20% at the blue wavelengths, decreasing to as low as 11% in the blue-green to green wavebands. These results, however, do not meet satellite ocean color goals of estimating $L_{wn}(\lambda)$ to within 5%. Nonetheless, these relatively small differences are quite remarkable given the extreme difficulties in accurately measuring $L_w(\lambda)$ *in situ* and remotely.

Our study shows that existing and future buoy-mooring systems are and will be essential to ocean color validation and vicarious calibration. However, buoy-mooring systems alone are not the complete answer as they only provide documentation of discrepancies, not solutions. Future observational platform systems must include, for example, robust measurements relating to atmospheric optical and environmental conditions. Optical data from a wide variety of oceanic environments and complementary interdisciplinary data for comparative analyses are essential to continuing improvements to the quality of satellite ocean color data and associated algorithms for the derivation of environmentally important biogeochemical parameters (IOCCG, 1998, 1999, 2000, 2004, 2006).

Acknowledgements

The Bermuda Testbed Mooring (BTM) during the time period of interest (Deployment #12) was supported by the NSF Ocean Technology and Interdisciplinary Coordination Program, NSF Chemical Oceanography Program, and NSF Biological Oceanography Program (TD: OCE-9627281, OCE-9730471, OCE-9819477), NASA (TD: NAS5-97127), the ONR Ocean Engineering and Marine Systems Program (DF: N00014-96-1-0028 and N00014-94-1-0346), and the University of California, Santa Barbara. Derek Manov and Frank Spada of OPL are thanked for providing expert engineering and technical support of the BTM and its optical instruments used for this study. Special thanks are extended to John Kemp for his dedication to the BTM, and to the Captain and crew of the R/Vs Weatherbird II and Atlantic Explorer for their continuing assistance at sea.

References

Abbott, M. R. and R. M. Letelier (1998): Decorrelation scales of chlorophyll as observed from bio-optical drifters in the California Current. *Deep-Sea Res. II*, **45**, 1639–1667.

Aiken, J., G. F. Moore and P. M. Holligan (1992): Remote sensing of oceanic biology in relation to global climate change. *J. Phycol.*, **28**, 579–590.

Austin, R. W. (1974): The remote sensing of spectral radiance from below the ocean surface. p. 317–344. In *Optical Aspects of Oceanography*, ed. by N. G. Jerlov and E. S. Nielson, Academic.

Barnes, R. A., R. E. Eplee, G. M. Schmidt, F. S. Patt and C. R. McClain (2001): The calibration of SeaWiFS, Part 1: direct techniques. *Appl. Opt.*, **40**, 6682–6700.

Behrenfeld, M. J. and P. G. Falkowski (1997): A consumer's guide to phytoplankton primary productivity models. *Limnol. Oceanogr.*, **42**, 1479–1491.

Behrenfeld, M. J., E. Boss, D. A. Siegel and D. M. Shea (2005): Carbon-based ocean productivity and phytoplankton physiology from space. *Global Biogeochem. Cycles*, **19**, GB1006, doi:10.1029/2004GB002299.

Campbell, J., D. Antoine, R. Amstrong, K. Arrigo, W. Balch, R. Barber, M. Behrenfeld, R. Bidigare, J. Bishop, M. Carr, W. Esaias, P. Falkowski, N. Hoepffner, R. Iverson, D. Kiefer, S. Lohrenz, J. Marra, A. Morel, J. Ryan, V. Vedemikov, K. Waters, C. Yentsch and J. Yoder (2002): Comparison of algorithms for estimating ocean primary production from surface chlorophyll, temperature, and irradiance. *Global Biogeochem. Cycles*, **16**, 1–15.

Chang, G. C. and R. W. Gould, Jr. (2006): Comparisons of optical properties of the coastal ocean derived from satellite ocean color and in situ measurements. *Opt. Exp.*, **14**, 10,149–10,163.

Chang, G. C., E. Boss, C. Mobley, T. D. Dickey and W. S. Pegau (2003): Toward closure of upwelling radiance in coastal waters. *Appl. Opt.*, **42**, 1574–1582.

Chavez, F. P., J. T. Pennington, R. Herlien, H. Jannasch, G. Thurmond and G. E. Friederich (1997): Moorings and drifters for real-time interdisciplinary oceanography. *J. Atmos. Oceanic Technol.*, **14**, 1199–1211.

Chavez, F. P., P. D. Wright, R. Herlien, M. Kelley, F. Shane and P. G. Strutton (2000): A device for protecting moored spectroradiometers from biofouling. *J. Atmos. Oceanic Technol.*, **17**, 215–219.

Clark, D. K., H. R. Gordon, K. J. Voss, Y. Ge, W. Broenkow and C. Trees (1997): Validation of atmospheric correction over the oceans. *J. Geophys. Res.*, **102**, 17,209–17,217.

Clark, D. K., M. A. Yarbrough, M. Feinholz, S. Flora, W. Broenkow, Y. S. Kim, B. C. Johnson, S. W. Brown, M. Yuen and J. L. Mueller (2003): MOBY, a radiometric buoy for performance monitoring and vicarious calibration of satellite ocean color sensors: measurement and data analysis protocols. In *Ocean Optics Protocols for Satellite Ocean Color Sensor Validation, Volume VI*, ed. by J. L. Mueller, G. S. Fargion and C. R. McClain, NASA/TM-2003-211621, NASA Goddard Space Flight Center.

Dickey, T. D. (2003): Emerging ocean observations for interdisciplinary data assimilation systems. *J. Mar. Syst.*, **40–41**, 5–48.

Dickey, T., D. Frye, H. Jannasch, E. Boyle, D. Manov, D. Sigurdson, J. McNeil, M. Stramska, A. Michaels, N. Nelson, D. Siegel, G. Chang, J. Wu and A. Knap (1998): Initial results from the Bermuda Testbed Mooring Program. *Deep-Sea Res. I*, **45**, 771–794.

Dickey, T. D., S. Zedler, D. E. Frye, H. Jannasch, D. Manov, D. Sigurdson, J. D. McNeil, L. Dobeck, X. Yu, T. Gilboy, C. Bravo, S. C. Doney, D. A. Siegel and N. Nelson (2001): Physical and biogeochemical variability from hours to years at the Bermuda Testbed Mooring site: June 1994–March 1998. *Deep-Sea Res. II*, **48**, 2105–2131.

Dickey, T. D., G. C. Chang and M. R. Lewis (2006): Optical oceanography: recent advances and future directions using global remote sensing and in situ observations. *Rev. Geophys.*, **44**, RG1001, doi:10.1029/2003RG000148.

Fargion, G. S. and J. L. Mueller (2000): Ocean optics protocols for satellite ocean color sensor validation, rev. 2. In *NASA Technical Memo*, 2000-209966, NASA Goddard Space Flight Center.

Frouin, R., D. W. Lingner, C. Gautier, K. S. Baker and R. C. Smith (1989): A simple analytical formula to compute clear sky total and photosynthetically available solar irradiance at the ocean surface. *J. Geophys. Res.*, **94**, 9731–9742.

Gordon, H. R. and K. Ding (1992): Self-shading of in-water optical instruments. *Limnol. Oceanogr.*, **37**, 491–500.

Hooker, S. B. and C. R. McClain (2000): The calibration and validation of SeaWiFS data. *Prog. Oceanogr.*, **45**, 427–465.

Hooker, S. B., W. E. Esaias, G. C. Feldman, W. W. Gregg and C. R. Maclain (1992): SeaWiFS Technical Report Series, An Overview of SeaWiFS and Ocean Color. p. 24. In *NASA Technical Memorandum*, 104566, Vol. 1, NASA Goddard Space Flight Center.

IOCCG Report Number 1 (1998): Minimum requirements for an operational ocean-colour sensor for the open ocean. p. 46. In *International Ocean Colour Coordinating Group*, ed. by A. Morel.

IOCCG Report Number 2 (1999): Status and plans for satellite ocean-colour missions: Considerations for complementary missions. p. 43. In *International Ocean Colour Coordinat-*

ing Group, ed. by J. A. Yoder.

IOCCG Report Number 3 (2000): Remote sensing of ocean colour in coastal and other optically-complex waters. p. 140. In *International Ocean Colour Coordinating Group*, ed. by S. Sathyendranath.

IOCCG Report Number 4 (2004): Guide to the creation and use of ocean-colour, Level-3, binned data products. p. 88. In *International Ocean Colour Coordinating Group*, ed. by D. Antoine.

IOCCG Report Number 5 (2006): Remote sensing of inherent optical properties: Fundamentals, tests of algorithms, and applications. p. 126. In *International Ocean Colour Coordinating Group*, ed. by Z.-P. Lee.

Ishizaka, J., I. Asanuma, N. Ebuchi, H. Fukushima, H. Kawamura, K. Kawasaki, M. Kishino, M. Kubota, H. Masuko, S. Matsumura, S. Saitoh, Y. Senga, M. Shimanuki, N. Tomii and M. Utashima (1997): Time series of physical and biological parameters off Shimane, Japan, during fall of 1993: First observation by moored optical buoy system for ADEOS data verification. *J. Oceanogr*., **53**, 245–258.

Kirk, J. T. O. (1994): *Light and Photosynthesis in Aquatic Ecosystems*. 2nd ed., Cambridge University.

Kishino, M., J. Ishizaka, S. Saitoh, Y. Senga and M. Utashima (1997): Verification plan of OCTS atmospheric correction and phytoplankton pigment by moored optical buoy system. *J. Geophys. Res*., **102**, 17,197–17,207.

Kuwahara, V. S., P. G. Strutton, T. D. Dickey, M. R. Abbott, R. M. Letelier, M. R. Lewis, S. McLean, F. P. Chavez, A. H. Barnard and J. R. Morris (2003): Radiometric and bio-optical measurements from moored and drifting buoys: measurement and data analysis protocols. p. 35–79. In *Ocean Optics Protocols for Satellite Ocean Color Sensor Validation, Revision 4, Vol. VI: Special Topics in Ocean Optics Protocols and Appendices*, ed. by J. L. Mueller, G. S. Fargion and C. R. McClain, NASA/TM-2003-21621, NASA Goddard Space Flight Center.

Letelier, R. M., D. M. Karl, M. R. Abbott, P. Flament, M. Freilich, R. Lukas and T. Strub (2000): Role of late winter mesoscale events in the biogeochemical variability of the upper water column of the North Pacific Subtropical Gyre. *J. Geophys. Res*., **105**, 28,723–28,739.

Manov, D. V., G. C. Chang and T. D. Dickey (2004): Methods for reducing biofouling of moored optical sensors. *J. Atmos. Oceanic Technol*., **21**, 957–967.

Mobley, C. D. (1994): *Light and Water: Radiative Transfer in Natural Waters*. Academic.

Morel, A. (1991): Light and marine photosynthesis: A spectral model with geochemical and climatological implications. *Prog. Oceanogr*., **26**, 263–306.

Morel, A. and S. Maritorena (2001): Bio-optical properties of oceanic waters: A reappraisal. *J. Geophys. Res*., **106**, 7163–7180.

Mueller, J. L. and R. Austin (2003): Characterization Oceanographic and Atmospheric Radiometers. p. 17–33. In *Ocean Optics Protocols for Satellite Ocean Color Sensor Validation, Revision 4, Vol. II: Instrument Specifications, Characterization and Calibration*, ed. by J. L. Mueller, G. S. Fargion and C. R. McClain, NASA/TM-2003-21621, NASA Goddard Space Flight Center.

O'Reilly, J., S. Maritorena, B. G. Mitchell, D. Siegel, K. L. Carder, S. Garver, M. Kahru and C. McClain (1998): Ocean color chlorophyll algorithms for SeaWiFS. *J. Geophys. Res*., **103**, 24,937–24,953.

Pinkerton, M. H., S. J. Lavender and J. Aiken (2003): Validation of SeaWiFS ocean color satellite data using moored databuoy. *J. Geophys. Res*., **108**, 3133, doi:10.1029/2002JC001337.

Pope, R. M. and E. S. Fry (1997): Absorption spectrum (380–700 nm) of pure water. II. Integrating cavity measurements. *Appl. Opt*., **36**, 8710–8723.

Prieur, L. and S. Sathyendranath (1981): An optical classification of coastal and oceanic waters based on the specific spectral absorption curves of phytoplankton pigments, dissolved organic matter, and other particulate materials. *Limnol. Oceanogr*., **26**, 671–689.

Spada, F. W., D. V. Manov and G. Chang (2007): Interdisciplinary ocean sensor technology development. *Sea Tech*., March, 31–35.

Strutton, P. G., J. P. Ryan and F. P. Chavez (2001): Enhanced chlorophyll associated with tropical instability waves in the equatorial Pacific. *Geophys. Res. Lett*., **28**, 2005–2008.

Zaneveld, J. R. V., E. Boss and P. A. Hwang (2001): The influence of coherent waves on the remotely sensed reflectance. *Opt. Exp*., **9**, 260–266.

Zheng, X., T. Dickey and G. Chang (2002): Variability of the downwelling diffuse attenuation coefficient with consideration of inelastic scattering. *Appl. Opt*., **41**, 6477–6488.